Journal of Fluids and Structures 133 (2025) 104225

Contents lists available at ScienceDirect

Journal of Fluids and Structures

journal homepage: www.elsevier.com/locate/jfs

Uncertainty quantification and sensitivity analysis of the SST turbulence model applied to VIV

Simone Martini [a], Mitja Morgut [a], Riccardo Pigazzini [b,*], Lucia Parussini [a]

[a] Department of Engineering and Architecture, University of Trieste, Piazzale Europa 1, 34127 Trieste, Italy
[b] Department of Industrial Engineering, University of Naples Federico II, Via Claudio 21, 80125 Naples, Italy

ARTICLE INFO

Keywords:
VIV
URANS
CFD
OpenFOAM
UQ
Sobol

ABSTRACT

This paper presents the results of an Uncertainty Quantification and Sensitivity Analysis carried out for the $k-\omega$ SST turbulence model applied to the bi-dimensional study of Vortex Induced Vibrations of an elastically mounted cylinder. The turbulence model parameters are treated as epistemic uncertain variables and the forward propagation of uncertainty is evaluated using stochastic expansions based on non-intrusive polynomial chaos. The relative contribution of the closure coefficients to the total uncertainty of the output quantities of interest, the non-dimensional amplitude and the frequency ratio, is evaluated using the Sobol indices. The analysis is repeated for different orders of the polynomial chaos expansion. A set of significant coefficients, which contribute most to the uncertainty for this specific case is identified, and furthermore compared with the sets provided for some other selected flow problems in order to gain further insight on the $k-\omega$ SST turbulence model.

1. Introduction

Vortex Induced Vibrations (VIV) occur when shedding vortices induce an oscillatory force on a blunt structure in steady or unsteady flow mostly in the direction perpendicular to the flow. If the structure is free to move or is partially restrained by *equivalent springs*, the body starts oscillating. Large oscillations are typically observed if the structure is subjected to near-resonance excitation. This occurs when there is the quasi-synchronization between vortex shedding frequency and natural frequency of the system. In such conditions, the amplitude may be of the same order of the size of the body, depending on several parameters. The stiffness of the restoring mechanism, the mechanical damping, mass ratio and Reynolds number (Re) being some of them.

The VIV problem on circular cylinders arises in many fields of engineering. Among others, tube-and-shell heat exchangers (Weaver and Fitzpatrick, 1988), coastal and marine applications such as pipe risers (Le Cunff et al., 2002; Zheng et al., 2014), mooring lines, spar, TLPs (Drumond et al., 2018) offshore wind turbines (Yin et al., 2022) etc. VIV phenomenon has been studied also to develop renewable energy technology, using one or more oscillating cylinders in tandem configuration in order to generate electricity (Bernitsas et al., 2008; Hobbs and Hu, 2012; Soti et al., 2017).

To understand, predict and prevent VIV phenomenon, a large amount of experimental and numerical research has been carried out.

Regarding the numerical simulations, it is important to point out that in the case of a high-Re flow conditions the vortex-wake around circular cylinders is in general three-dimensional and thus the results from 2D numerical studies (Guilmineau and Queutey (2004), Pan et al. (2007), Wanderley et al. (2008), Wu et al. (2014) and Pigazzini et al. (2018)) could not match experimental data

* Corresponding author.
E-mail addresses: martini.sim@me.com (S. Martini), mmorgut@units.it (M. Morgut), riccardovasco.pigazzini@unina.it (R. Pigazzini), lparussini@units.it (L. Parussini).

https://doi.org/10.1016/j.jfluidstructs.2024.104225
Received 22 January 2024; Received in revised form 31 August 2024; Accepted 10 November 2024
Available online 18 December 2024

for all the considered range of flow velocity. Nevertheless, the majority of 3D VIV simulations of circular cylinders concern with low-Re flows due to the difficulties given by the expensive hardware requirements and extra modelling efforts to properly describe the fluid flow beyond the laminar region.

Application of low-Re simulations is arguable, since the flow around marine structures, which present submerged cylindrical structures (pipe and cables) and other civil engineering applications is in the range between $\mathrm{Re} = 10^4$ and $\mathrm{Re} = 10^6$, for instance. Therefore, also due to the ever-increasing availability of computational resources, the numerical study of the VIV phenomenon at higher Reynolds number has gained increased interest.

One of the first attempts of a 3D numerical simulation of a cylinder VIV at high-Re is found in the work of Saltara et al. (2011), using 3D Detached Eddy Simulations (DES). Despite the use of a high fidelity model, in order to simulate one degree of freedom (1-DOF) VIV of a circular cylinder with a low mass-damping parameter at $\mathrm{Re} = 10^4$, their simulation results only partially agreed with the experimental results.

Other scale resolving methods such as Direct Numerical Simulation (DNS) and Large Eddy Simulation (LES) have been employed, but generally for lower Reynolds number cases.

For instance, Blackburn et al. (2001), performed both 2D and 3D DNS simulations of low vortex-induced vibration at low-Re ($\mathrm{Re} = 3900$). A reasonable agreement between 3D simulations and experiments was found, where the amplitude response of 2D simulations did not show any sign of an upper branch. Given that, they concluded that 2D simulations were inadequate for modelling high-Re vortex-induced vibration (VIV). The main issue is that they had difficulties in obtaining high-Re values in the DNS simulation, on one hand, and low values of Re in experiments, on the other, have highlighted the limitations of this comparison between the numerical and the experimental results.

The 3D DNS sudy of Lucor et al. (2005) at 1-DOF VIV for three different Reynolds numbers: $\mathrm{Re} = 1000$, 2000 and 3000 show that results were comparable to the experiments, and the influence of Re was also highlighted. The results of the 1-DOF VIV showed the effect of the location and magnitude of upper branch amplitude response respect to Re. A sharp drop in the spanwise correlation factor of wake and forces near the transition between the upper and lower branches is also observed along with the existence of hysteresis between the two branches.

Al-Jamal and Dalton (2004) performed both 2D and 3D LES VIV simulations of a two degree of freedom (2-DOF) circular cylinder at $Re = 8000$. Pastrana et al. (2018) also performed 2-DOF VIV LES simulations for three different subcritical Reynolds numbers and found good agreement with experimental results for what concerns the transversal oscillation amplitudes, as well as with the different vortex structures.

Recently, Li and Ishihara (2021) compared the results obtained with both 3D LES and 2D Reynolds Averaged Naviers Stokes (RANS) approaches for the 2-DOF VIV of a circular cylinder. Results show that 3D LES, by taking fifty times the computational effort respect to the 2D RANS simulations – carried out employing the Shear Stress Transport (SST) turbulence model – provides much better estimation of the transversal amplitude, although only in the upper branch.

As for the 1-DOF case, recently, Martini et al. (2021) in the context of RANS simulations explored the differences between the 2D and 3D simulations. The study has been carried out employing the $k-\omega$ SST turbulence model and conducting the simulations for different flow regimes alternatively on bi — and three dimensional meshes. The results point out that that the 2D RANS simulation can be considered consistent with 3D RANS simulations in some of the flow regimes, in particular in so-called *lower branch regime*.

Therefore, considering only the *lower branch regime*, in this study, we exploit the opportunity of performing an uncertainty analysis for a VIV case with the use of two-dimensional computational grids.

At this stage, considering the context of this study, it is important to point out that in fluid mechanics, the study of turbulence, due to the chaotic nature of the phenomenon, remains one of the most intriguing topic. In order to predict turbulent flows in Computational Fluid Dynamics (CFD) the lack of the physical knowledge has imposed to introduce, in the context of RANS simulations, turbulence models with several constraints, namely closure coefficients, in order to balance the model equations.

The closure coefficients are determined by using a combination of heuristic and empirical approaches, typically from the use of experimental data. Thus, in recent years, uncertainty quantification techniques have also been applied to different flow cases in order to quantify the uncertainty related to turbulence models. In this respect, a very comprehensive review of studies carried out for RANS turbulence models is provided in Xiao and Cinella (2019), while information regarding the most common techniques are available in Xiu (2010), Sullivan (2015), Bigoni (2015), Soize (2017).

Here, in order to introduce the current study, we briefly point out that uncertainty quantification methods can be classified as intrusive and non-intrusive. Non-intrusive UQ methods offer a powerful approach for quantifying uncertainties without modifying the original model (often referred to as the full-order model, FOM), making it easier to implement compared to intrusive methods. By leveraging existing models and data analysis techniques, they enable efficient quantification of uncertainties and provide valuable insights into system behaviour under various conditions. This provides several advantages, especially when dealing with computationally expensive simulations.

Furthermore, in the context of intrusive methods, it is possible to distinguish between sampling-based methods and spectral methods.

Sampling-based methods are the most robust uncertainty techniques available. They are applicable to a wide range of problems, including nonlinear and high-dimensional ones, but they primarily provide statistical information (mean, variance) and not analytical expressions for the output, making them less suitable for sensitivity analysis. Moreover, these methods could be impracticable in case of computational demanding simulations. As a matter of fact, sampling-methods (Monte Carlo Methods) are often regarded as the last means to solve uncertainty quantification (UQ) problems in engineering practice because of its prohibitive computing cost and time span (Xia et al., 2021).

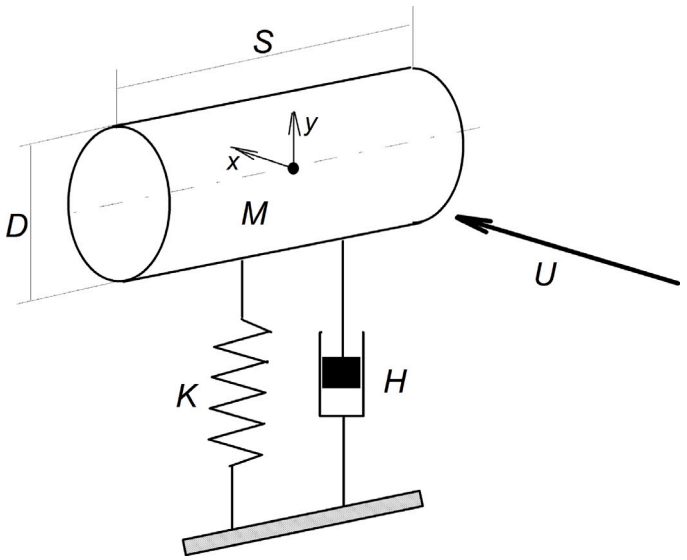

Fig. 1. Schematic representation of VIV problem and relevant symbols.

In order to overcome possible limitation related to available computational resources alternative approaches can be employed. In spectral methods, such is Polynomial Chaos Expansions (PCE), the uncertain output of the FOM is expressed as a polynomial expansion of the uncertain input parameters. This method is efficient for low-dimensional problems and provides the analytical expressions for the output allowing for calculation of moments (mean, variance) and sensitivity analysis to understand how input uncertainties affect the output.

Moreover, surrogate models such as Gaussian Process Regression (GPR) could also be used. This approach often provides more accurate results compared to PCE for complex problems. But, the GPR model training can be computationally expensive, especially with large datasets, and it creates a statistical model without providing analytical expressions for the output, making it challenging to interpret sensitivity and understand the underlying relationships. Based on this approach, Rezaeiravesh et al. (2022) recently proposed a framework applicable to any computational physics problem.

Considering the interest in the uncertainty quantification of turbulence models, in this study, we have evaluated the forward propagation of the uncertainties of the $k-\omega$ SST turbulence model closure coefficients 1-DOF VIV of a rigid circular cylinder. As pointed out before, we remark that the study has been carried out considering 2D flow regimes (Martini et al., 2021).

Since we have considered a computationally expensive CFD problem, the Non-Intrusive Polynomial Chaos Method (NIPC) has been used in combination with the Sobol indices (Sudret-2008, 2008; Ghanem et al., 2017) to rank the relative contribution of turbulence model coefficients to the total uncertainty.

The study has been carried with different polynomial orders ($p = 2,3,4,5$). In the case of $p = 4,5$ an additional reduced dimensional analysis (RDA) has been applied.

From the overall results it emerges that, for this specific case, the $k-\omega$ SST turbulence model coefficients which contribute most to the uncertainty of the considered quantities of interest (for brevity, QoIs), adimensional amplitude and frequency ratio, are: σ_{ω_2}, β^*/β_2, κ, a_1.

In the following, an overview of the test case used as reference data is presented in Section 2.

In Section 3 the description of the CFD simulations is given.

In Section 4, the Uncertainty Quantification (UQ) and sensitivity analysis (SA) methodology is presented.

In Section 5, the results obtained from the current study are discussed. A comparison with some other selected flow problems is also presented. Finally, the conclusion are provided.

2. Problem description

In this work we consider a rigid circular cylinder of mass M, with a diameter D and span S, free to move in transversal direction respect to a uniform cross flow U. The cylinder is considered mounted on a linear spring and a weak linear damper. The system is sketched in Fig. 1 where the spring stiffness and the mechanical damping of the system are identified with K and H, respectively.

The dimensionless dynamic parameters, considered in this study, are those of the experimental setup of Khalak and Williamson (1996). The experimental studies were characterized by low mass ratio $m^* = M/(\rho\pi D^2 S/4) = 2.4$ and low damping ratio $\zeta = H/H_{critical} \approx 0.0054$. $H_{critical}$ is the critical damping of a linear mass–spring-damper system. Further definitions and details are listed in Table 1.

In order to vary the reduced velocity $U^* = U/(f_0 D)$, the uniform (free-stream) cross flow velocity U has been set to different initial value while the natural frequency of the system in still fluid f_0 has been kept constant.

Table 1
System properties.

Description	Symbol	Value
Cylinder diameter	D (m)	0.0381
Mass ratio	$m^* = M/(\rho \frac{\pi D^2}{4} S)$	2.4000
Damping ratio	$\zeta = H/(2\sqrt{K(M+M_A)})$	0.0054
Added mass coefficient	$C_A = M_A/(\rho \frac{\pi D^2}{4} S)$	1.0000
Mass-damping parameter	$m^* \zeta$	0.0130
Natural frequency in air	$f_{0,a} = \frac{1}{2\pi}\sqrt{\frac{K}{M}}$ (Hz)	0.7846
Natural frequency in water	$f_0 = \frac{1}{2\pi}\sqrt{\frac{K}{M+M_A}}$ (Hz)	0.6592

Table 2
Selected system parameters.

Description	Symbol	Value
Cylinder span	S (m)	0.0250
Cylinder mass	M (kg)	0.0683
Spring stiffness	K (N/m)	1.6609
Structural damping	H (N/(m/s))	0.0043

3. Simulations setup

The required numerical simulations have been carried out using a native URANS solver (pimpleDyMFoam) available in the OpenFOAM CFD toolbox (release 2.4).

The $k-\omega$ SST turbulence model has been used to close the system of the governing equations, and the simulations have been carried out exclusively for three reduced velocities ($U^* = 7, 8, 9$) of the lower branch. This range of reduced velocities, corresponds to sub-critical Reynolds numbers in the range of 5.8×10^3 to 7.5×10^3.

The simulations have been carried out considering the computational domain depicted in Fig. 2 while Table 2 summarized the system properties. The simulations have been performed using fresh water. The coupling between the rigid body motion and the fluid flow has been explicit. The Arbitrary Lagrangian–Eulerian (ALE) method has been used to follow the mesh motion (Löhner and Yang, 1996), the displacement of the internal nodes has been computed from the boundary motions by means of the Laplace equation with variable diffusivity based on inverse distance. The 2nd order upwind scheme has been used for the discretization of the advective terms while the first order implicit Euler method, coupled with the dynamically adjustable stepping technique (Lysenko et al., 2014), has been used for time integration. To achieve stable and convergent calculations for every time step, a maximum Courant number Co less than 0.9 has been adopted.

Free-stream velocity, constant static pressure and no-slip condition have been set on the inlet, outlet and body boundary conditions respectively. As for the detailed description of boundary and initial condition we refer to Pigazzini (2016). However, here, for the sake of clarity (considering the context of the study) we point out that the values of the turbulence kinetic energy and turbulence frequency, imposed on the inlet boundary, have been set as $k = 0.1U^2/Re_L$ and $\omega = 10U/L$ following Menter's approach (Menter, 1994).

We clarify that in OpenFOAM (release 2.4) the implemented version of the $k-\omega$ SST model, (reported in Appendix for the sake of convenience) is a variant of the original model presented by Menter (1994). It embraces the improvements proposed (Menter and Esch, 2001) with the updated coefficients (Menter et al., 2003b) but with the consistent production terms from Menter and Esch (2001)[1] and the addition of a new term that considers rough walls, as proposed by Hellsten (1997).

As a matter of fact, in this version, the closure coefficients, also include γ_1 and γ_2 which are evaluated, in function of the other model constants as:

$$\begin{aligned} \gamma_1 &= \beta_1/\beta^* - \sigma_{\omega_1}\kappa^2/\sqrt{\beta^*} \\ \gamma_2 &= \beta_2/\beta^* - \sigma_{\omega_2}\kappa^2/\sqrt{\beta^*} \end{aligned} \tag{1}$$

Since the simulations have been carried out considering a smooth cylinder surface, the auxiliary function F_3, designed to prevent the SST limitation from being activated in the roughness layer in rough wall, has been switched off in every simulation. The constants b_1 (constant factor in the turbulent viscosity equation) and c_1 (constant factor in the production limiter) has been fixed to 1 and 10 respectively.

It is important to clarify that using the solver pimpleDyMFoam it is not possible to perform simulations using *pure* 2D meshes, i.e. computational grids composed of bi-dimensional elements. As a matter of fact, here, 2D meshes are intended as 3D meshes composed by a single layer of cells normal to the XY plane, with thickness equal to cylinder span, $S = 2.50 \times 10^{-2}$ m.

[1] As noted by the Largley Research Center (NASA Langley Research Center, 2021) in Menter et al. (2003b) articles there is a typo in the omega equation therefore in OpenFOAM is implemented the corrected version.

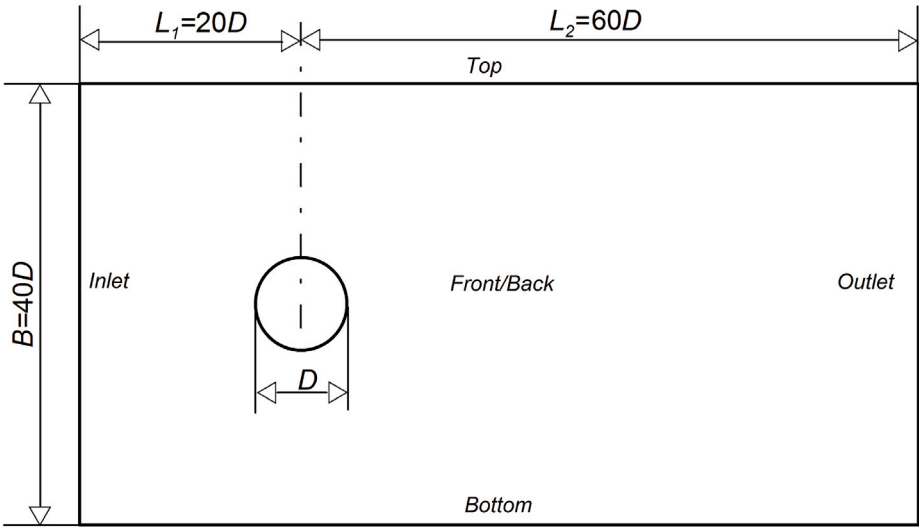

Fig. 2. Computational domain.

Table 3
Grid information.

Description	Value
Cells	38 188
Faces	153 603
Points	78 078
Add layer setup	
Number of surface layers	35
Minimum thickness	$6.214 \cdot 10^{-5}$
Cylinder circumference points	56
Grid expansion factor	1.078
Mesh quality	
Maximum cell aspect ratio	13.285
Maximum mesh non-orthogonality	33.804
Maximum skewness	0.444

The mesh generation utility, *snappyHexMesh*, supplied with OpenFOAM has been used in setting up the grids. The *snappyHexMesh* utility provides a flexible solution during the meshing process thanks to the specific mesh refinement region inside the domain.

The centre of cylinder has been taken as origin. The near-wall grid spacing has bee designed to ensure the first cell in the viscous sub-layer, in order to avoid the $y^+ \approx 1$ condition. For the off-wall region, grids have two concentric levels of higher resolution. An additional refinement box, spanning from the centre of cylinder to the outlet boundary of the domain, has been added in order to correctly resolve the wake field. Finally, to avoid an abrupt change in grid spacing between two neighbour cells, the number of buffer layers between different refinement levels has been set to 4. Table 3 summarizes the main characteristics of the 2D mesh used. In Fig. 3 the computational mesh, in the XY plane view, is depicted, showing the refinement close to the cylinder surface.

The number of cells and refinement have been determined in a preliminary study (Martini, 2020). Furthermore, the results of 2D URANS simulations were compared with both the experimental data and the results of 3D URANS simulations in Martini et al. (2021). Regarding this comparison, the results of the cylinder response (in terms of non-dimensional amplitude $A^* = A/D$ and its non-dimensional frequency $f^* = f/f_0$) are shown in Figs. 4(a) and 4(b) respectively.

As shown in Fig. 4(a), bi-dimensional simulations did not present important discrepancies with the experiments, the differences between 2D and 3D meshes (simulations) are most visible in the initial and upper branches, notable differences are also observed in the initial part of desynchronization range. The cylinder frequency response of 2D and 3D simulations compares very well with experimental data in Fig. 4(b). In particular, also some double-peaked behaviour in the initial branch has been successfully simulated.

As highlighted by Martini et al. (2021) the complexity of the phenomenon in the upper branch region would probably require more sophisticated and computationally demanding 3D simulation. Therefore, for the present study, we have considered only three reduced velocities ($U^* = 7, 8, 9$) of the lower branch, where there is a good comparison between experimental data and the 2D and 3D solutions.

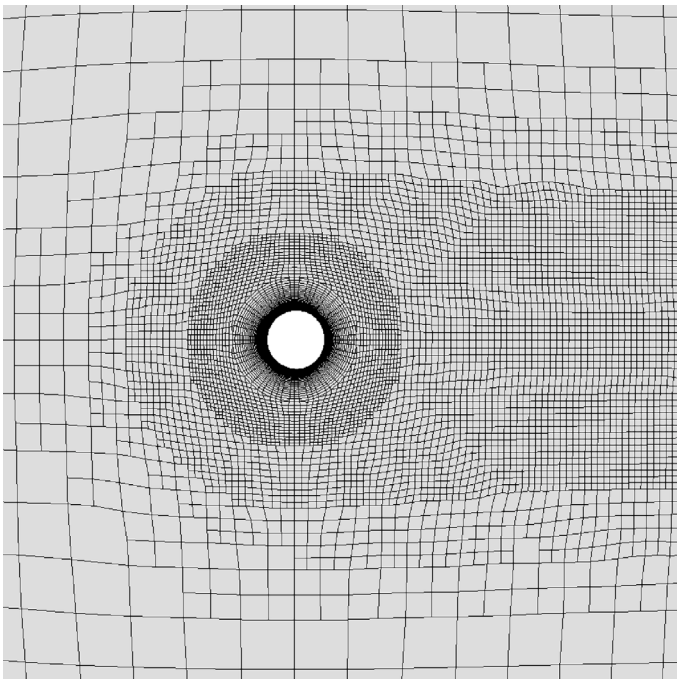

Fig. 3. 2D grid structure and its detail.

4. UQ and sensitivity analysis methodology

Here it is assumed that the values of the model closure coefficients are uncertain and the goal is to quantify the effect of these uncertainties on the URANS flow solution using UQ theory.

The uncertainties in computational models can be treated as aleatory or epistemic. Aleatory uncertainties represent inherent variations in a system, whereas epistemic uncertainties arise due to lack of knowledge. In this study, all turbulence model coefficients are treated as epistemic uncertain variables due to the lack of a complete physical understanding of turbulence.

This section provides the details of the polynomial chaos techniques used in this study with a description of the Legendre polynomials used in this study as the basis functions. The first part outlines the general non-intrusive polynomial chaos formulation with the point collocation approach. The second part describes the Sobol indices, global sensitivity indices, used to give a measure of sensitivity. Finally, a brief description of the implemented procedure is given.

4.1. Point-collocation non-intrusive polynomial chaos

In recent studies Sudret (2008), Schaefer et al. (2015), Erb and Hosder (2018), the polynomial chaos (PC) method has been used as a means of UQ over traditional methods, such as Monte Carlo, to reduce computational expense. The point-collocation Non-Intrusive Polynomial Chaos (NIPC) creates a surrogate model via least squares approach (i.e., polynomial response surface) by using the results of the CFD simulations performed on a proper number of collocation points determined using Latin Hypercube Sampling (LHS) methods for the propagation of uncertainty.

The PC is a stochastic method based on the spectral representation of the uncertainty. Following the explanation provided by West and Hosder (2015) an important aspect of spectral representation of uncertainty is that one may decompose a stochastic response function α^* (drag coefficient or pressure at a given point in the field as examples) into separable deterministic and stochastic components within a series expansion:

$$\alpha^*(\mathbf{x}, \boldsymbol{\varepsilon}) \approx \sum_{i=0}^{P_m} \alpha_i(\mathbf{x}) \Psi_i(\boldsymbol{\varepsilon}) \tag{2}$$

where α_i is the deterministic component and Ψ_i is the random variable basis function corresponding to the ith mode. Here, α^* is assumed to be a function of a deterministic independent variable vector $\mathbf{x}$, which includes the spatial coordinates and deterministic parameters of the problem, and of the n-dimensional standard random variable vector $\boldsymbol{\varepsilon} = (\varepsilon_0, \varepsilon_1, \ldots, \varepsilon_n)$. In theory, the polynomial chaos expansion (PCE) given by Eq. (2) should include infinite number of terms. However, in practical implementations, the

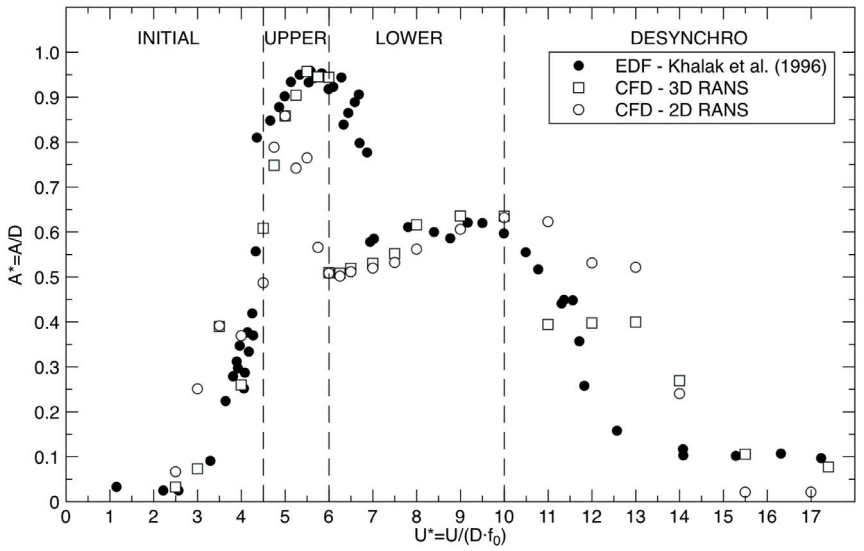

(a)

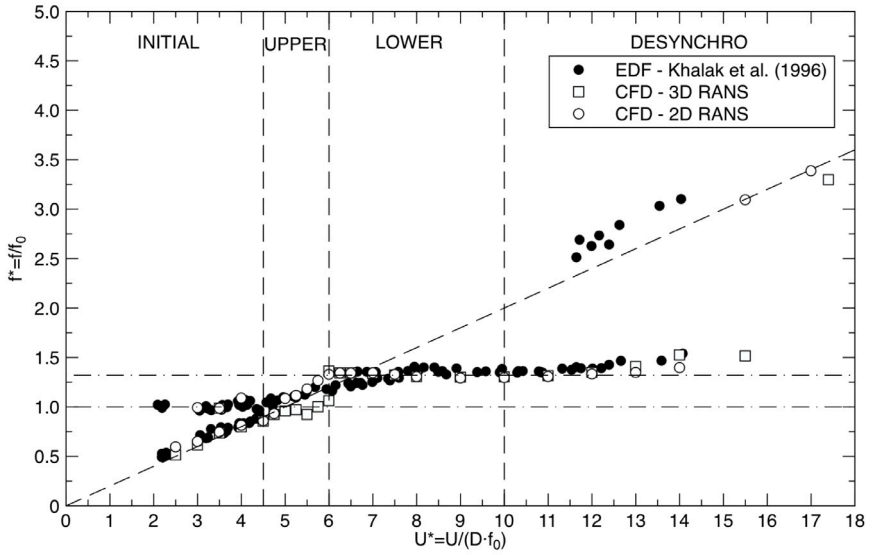

(b)

Fig. 4. Amplitude ratio $A^* = A/D$ (a) and frequency ratio $f^* = f/f_0$ (b) versus reduced velocity U^*. Comparison between experimental data by Khalak and Williamson (1996) (solid circles), present 2D CFD results (empty circles) and 3D CFD results by Martini et al. (2021) (empty squares). Vertical dashed lines marks the boundaries of branches in accordance with the CFD results. The oblique dashed line in (b) corresponds to St = 0.20.

expansion is truncated and a discrete sum is taken over a number of output modes (or total number of terms N_t) for a total-order expansion given by

$$N_t = P_m + 1 = \frac{(n+p)!}{n!p!}, \tag{3}$$

which is a function of the order of polynomial chaos p and the number of random dimensions n. The minimum number of samples, required to produce a response surface, could be assumed equal to N_t. However, Hosder et al. (2010) suggest multiplying N_t by an oversampling ratio $n_p = 2.0$ in order to obtain a better approximation to the statistics at each polynomial degree considered.

The basis functions, used in the stochastic expansion given in Eq. (2), are polynomials that are orthogonal with respect to a weight function over the support region of the input random variable vector.

The goal of the Non-Intrusive Polynomial Chaos methods is to obtain the deterministic polynomials coefficients treating the CFD code as a black box and performing the simulations considering a certain number of points of the random space (collocation points).

From the practical point of view, the collocation based NIPC method starts with replacing a stochastic response or a random function with its polynomial chaos expansion in Eq. (2). Then, a number of vectors ($\boldsymbol{\varepsilon}_i = \{\varepsilon_1, \varepsilon_2, \ldots, \varepsilon_n\}_i$), corresponding to the number of samples $N_s = n_p \cdot N_t$ ($\boldsymbol{\varepsilon}_i$, $i = 0, 1, \ldots, N_s - 1$), are chosen in random space and the CFD code is run in order to obtain responses at these points; this is the left-hand side of Eq. (2). With the left-hand side of Eq. (2). known from the solution of deterministic evaluations at the chosen random points, a linear system of N_s equations is formulated. This system is given by:

$$\begin{pmatrix} \alpha^*(\mathbf{x}, \varepsilon_0) \\ \alpha^*(\mathbf{x}, \varepsilon_1) \\ \vdots \\ \alpha^*(\mathbf{x}, \varepsilon_{(N_s-1)}) \end{pmatrix} = \begin{pmatrix} \Psi_0(\varepsilon_0) & \Psi_1(\varepsilon_0) & \ldots & \Psi_{P_m}(\varepsilon_0) \\ \Psi_0(\varepsilon_1) & \Psi_1(\varepsilon_1) & \ldots & \Psi_{P_m}(\varepsilon_1) \\ \vdots & \vdots & \ddots & \vdots \\ \Psi_0(\varepsilon_{(N_s-1)}) & \Psi_1(\varepsilon_{(N_s-1)}) & \ldots & \Psi_{P_m}(\varepsilon_{(N_s-1)}) \end{pmatrix} \begin{pmatrix} \alpha_0(\mathbf{x}) \\ \alpha_1(\mathbf{x}) \\ \vdots \\ \alpha_{P_m}(\mathbf{x}) \end{pmatrix}. \tag{4}$$

The spectral modes α_k of the random variable α^* are obtained by solving the linear system of Eq. (4).

When $n_p > 1.0$ the Eq. (4) is overdetermined and can be solved using a least squares approach.

4.2. Legendre polynomials

The *Legendre* polynomials are selected as a basis function in this study for their uniform and exponential input uncertainty distributions. The *Legendre* polynomials $Le_n(x)$ are the solutions of the following differential equation:

$$(1 - x^2)\ddot{y} - 2x\dot{y} + n(n+1)y = 0, \qquad n \in \mathbb{N}. \tag{5}$$

They may be generated by the following recurrence relationship:

$$Le_0(x) = 1, \tag{6}$$

$$(n+1)Le_{n+1}(x) = (2n+1)xLe_n(x) - nLe_{n-1}(x). \tag{7}$$

They are orthogonal with respect to the uniform probability measure over $[-1; 1]$:

$$\int_{-1}^{1} Le_m(x)Le_n(x)dx = \frac{2}{2n+1}\delta_{mn}, \tag{8}$$

where δ_{mn} is the Kronecker delta: $\delta_{mn} = 1$ if $m = n$ and 0 otherwise. If ε is a random variable with uniform Probability Density Function (PDF) over $[-1, 1]$, the following relationship holds:

$$E[Le_m(\varepsilon)Le_n(\varepsilon)] = \frac{1}{2n+1}\delta_{mn}, \tag{9}$$

where $E[.]$ is the mathematical expectation. The first three Legendre. e.g. the first three Le polynomials are:

$$Le_1(x) = x, \qquad Le_2(x) = \frac{1}{2}(3x^2 - 1), \quad Le_3(x) = \frac{1}{2}(5x^3 - 3x). \tag{10}$$

4.3. Sobol indices

Sobol indices (global nonlinear sensitivity indices) have been used to estimate the relative influence of individual closure coefficients and rank their relative contributions to the total uncertainty in the output quantities of interest.

Sobol indices can be derived via Sobol decomposition, which is a variance-based global sensitivity analysis method. This derivation utilizes the PCE coefficients calculated in Eq. (4). Therefore, the Sobol indices can be calculated analytically with almost no additional cost. Indeed, only elementary mathematical operations are needed to compute these indices from the expansion coefficients already calculated in Eq. (4).

To extract the Sobol indices, as a first step, the total variance D^T can be written in terms of PCE:

$$D^T = \sum_{j=1}^{P_m} \alpha_j^2(t, \mathbf{x})\langle\Psi_j^2(\boldsymbol{\varepsilon})\rangle. \tag{11}$$

Then, as shown by Sudret (Sudret, 2008) and Schaefer (Schaefer et al., 2015), the total variance can be decomposed as:

$$D^T = \sum_{i=1}^{i=n} D_i + \sum_{1\le i<j\le n}^{i=n-1} D_{i,j} + \sum_{1\le i<j<k\le n}^{i=n-2} D_{i,j,k} + \cdots + D_{1,2,\ldots,n}, \tag{12}$$

where the partial variances $D_{i_1,\ldots,i_s}$ are given by:

$$D_{i_1,\ldots,i_s} = \sum_{\beta\in i_1,\ldots,i_s} \alpha_\beta^2\langle\Psi_\beta^2(\boldsymbol{\varepsilon})\rangle, \qquad 1 \le i_1 < \cdots < i_s \le n. \tag{13}$$

The Sobol indices $S_{i_1,\ldots,i_s}$ are defined as,

$$S_{i_1,\ldots,i_s} = \frac{D_{i_1,\ldots,i_s}}{D^T}, \tag{14}$$

which satisfy the following equation:

$$\sum_{i=1}^{i=n} S_i + \sum_{1\le i<j\le n}^{i=n-1} S_{i,j} + \sum_{1\le i<j<k\le n}^{i=n-2} S_{i,j,k} + \cdots + S_{1,2,\ldots,n} = 1.0. \tag{15}$$

The Sobol indices provide a sensitivity measure due to individual contribution from each input uncertain variable (S_i), as well as the mixed contributions ($S_{i,j}, S_{i,j,k}, \ldots$). As shown by Sudret (2008), the total sensitivity indices (S_{T_i}) of an input parameter i have been defined in order to evaluate the total effect of an input parameter i. They are defined as the sum of the partial Sobol indices that include the particular parameter:

$$S_i^T = \sum_{L_i} \frac{D_{i_1,\ldots,i_s}}{D^T}; \qquad Le_i = \{(i_1,\ldots,i_s) : \exists k, 1 \le k \le s, i_k = i\}. \tag{16}$$

Note that Le_i corresponds to the polynomials depending only on parameter i.

For example, with $n = 3$, the total contribution to the overall variance from the first uncertain variable ($i = 1$) can be written as:

$$S_i^T = S_1 + S_{1,2} + S_{1,3} + S_{1,2,3}. \tag{17}$$

These formulations show that the Sobol indices can be used to provide a relative ranking of each input uncertainty to the overall variation in the output, in consideration of nonlinear correlation between input variables and output quantities of interest.

4.4. The logic of the implemented procedure

The uncertainty quantification study has been conducted with DAKOTA/UQ (Wojtkiewicz et al., 2001) (which is the uncertainty quantification component of DAKOTA (Design Analysis Kit for Optimization) version 6.10 (Eldred et al., 2006)) using stochastic expansions based on non-intrusive polynomial chaos. In this subsection the practical strategy employed in DAKOTA to drive the UQ analysis is provided. The proposed approach consists of three separated stages.

Stage 1 Using DAKOTA, the collocation points (samplings) for the deterministic CFD simulations are generated using LHS.

Stage 2 The overall CFD simulations are carried out for the given collocation points. The results are saved in proper text files.

Stage 3 Using DAKOTA, in combination with a proper ad hoc implemented interface, the polynomial chaos coefficients are determined based on the results obtained at stage 2 and the related probabilistic values as well as sensitivity indices are calculated.

Thanks to the numerical strategy described above, it is possible to perform the CFD simulations independently from DAKOTA which is only used at the first and third stages. Note that, at stage 2, DAKOTA, is not running.

5. Results and discussion

The two-step strategy proposed by Sudret (2008) has been used for the UQ of the turbulence model closure coefficients. In the two-step strategy, the first step consists of using a low order expansion (usually $p = 2$) in order to identify the most important variables. Then, in the second step, higher orders of expansion of a reduced model are considered in order to determine main sensitivity indices. Here, the first step analysis (Complete Coefficient Analysis) has been carried out using $p = 2, 3, 4$. The second step analysis (Reduces Coefficient Analysis) has been performed considering $p = 4, 5$

5.1. First step - complete coefficients analysis (CCA)

For the first step analysis, the forward propagation of uncertainty related to all model constants has been investigated within the ranges suggested by Schaefer et al. (2015) and reported in Table 4 for the sake of clarity.

The developed strategy has been systematically applied, increasing the order of the PCE ($p = 2, 3, 4$) to evaluate the possible effect of the polynomial order on the ranking of coefficients, for all the three different flow regimes.

Moreover, the oversampling ratio, $n_p = 2$, has always been used to provide a better approximation of the statistics at each polynomial degree considered. Therefore, the total computational cost (i.e. number of CFD evaluations required) has been $N_s = 110, 440$ and 1430 for $p = 2, 3, 4$ respectively.

The results from the current study have been compared with the available experimental data by Khalak and Williamson (1996). In particular, the results of the analyses in terms of mean value, standard deviation, minimum, and maximum of non-dimensional amplitude and non-dimensional frequency, are shown in Tables 5 and 6, where the results of the simulations carried out using native turbulence model coefficients (Base CFD) are also reported. From the overall results provided in Tables 5 and 6, it is possible to note that congruent results have been obtained among the analyses performed with different polynomial orders for all the considered flow regimes and both QoIs.

Table 4
$k-\omega$ SST closure coefficients and associated epistemic intervals.

Coefficient	Standard value	Lower bound	Upper bound
σ_{k_1}	0.85	0.7	1.0
σ_{k_2}	1.0	0.8	1.2
σ_{ω_1}	0.5	0.3	0.7
σ_{ω_2}	0.856	0.7	1.0
β^*/β_1	1.20	1.19	1.31
β^*/β_2	1.0870	1.05	1.45
β^*	0.09	0.0784	0.1024
κ	0.41	0.38	0.42
a_1	0.31	0.31	0.40

Table 5
Adimensional amplitude $A^* = A/D$, CCA results.

U^*	p	K.& W. (1996)	Base CFD	Mean	Std	Max	Min
	2			0.556	0.035	0.649	0.48
7	3	≈ 0.577	0.520	0.556	0.035	0.649	0.484
	4			0.555	0.035	0.677	0.447
	2			0.594	0.028	0.672	0.500
8	3	≈ 0.605	0.562	0.594	0.029	0.696	0.481
	4			0.591	0.030	0.704	0.477
	2			0.628	0.035	0.716	0.510
9	3	≈ 0.610	0.606	0.628	0.041	0.746	0.244
	4			0.627	0.036	0.753	0.247

Table 6
Frequency ratio $f^* = f/f_0$, CCA results.

U^*	p	K.& W. (1996)	Base CFD	Mean	Std	Max	Min
	2			1.330	0.013	1.389	1.312
7	3	≈ 1.258	1.294	1.331	0.015	1.377	1.312
	4			1.332	0.015	1.435	1.312
	2			1.310	0.008	1.337	1.300
8	3	≈ 1.407	1.307	1.311	0.008	1.350	1.299
	4			1.312	0.011	1.427	1.299
	2			1.296	0.008	1.324	1.288
9	3	≈ 1.392	1.346	1.299	0.027	1.765	1.288
	4			1.297	0.016	1.758	1.288

Considering Fig. 5 (left), where the main (first-order) Sobol indices obtained for A^* are compared, it is possible to note that the ranks corresponding to different polynomial orders are in line with each other.

Moreover, it is interesting to note that the coefficient a_1, which has the highest ranking for $U^* = 7$ and $U^* = 8$, is exceeded by $\sigma_{\omega 2}$ for $U^* = 9$. Finally, considering the overall results it is possible to note that, in this case, the coefficients that contribute the most to uncertainty are: $\sigma_{\omega 2}$, a_1, κ, β^*/β_2.

In case of f^* Fig. 5 (right) shows that also for this QoIs the ranking of the Sobol indices is congruent among the different polynomial orders. Also for f^* the model constant a_1 has the highest score for $U^* = 7$, however, differently from the case of A^* its contribution to uncertainty is almost negligible for $U^* = 9$. It is interesting to note that κ, for $U^* = 7$, has a similar score to $\sigma_{\omega 2}$, while its contribution is almost negligible for other reduced velocities. On the other hand, $\sigma_{\omega 2}$ plays a significant role in all the different flow regimes, especially for $U^* = 9$, where it clearly exhibits the highest score.

As a matter of fact, from the overall results, it is possible to note that $\sigma_{\omega 2}$ seems to play a significant role independently of the considered flow regime.

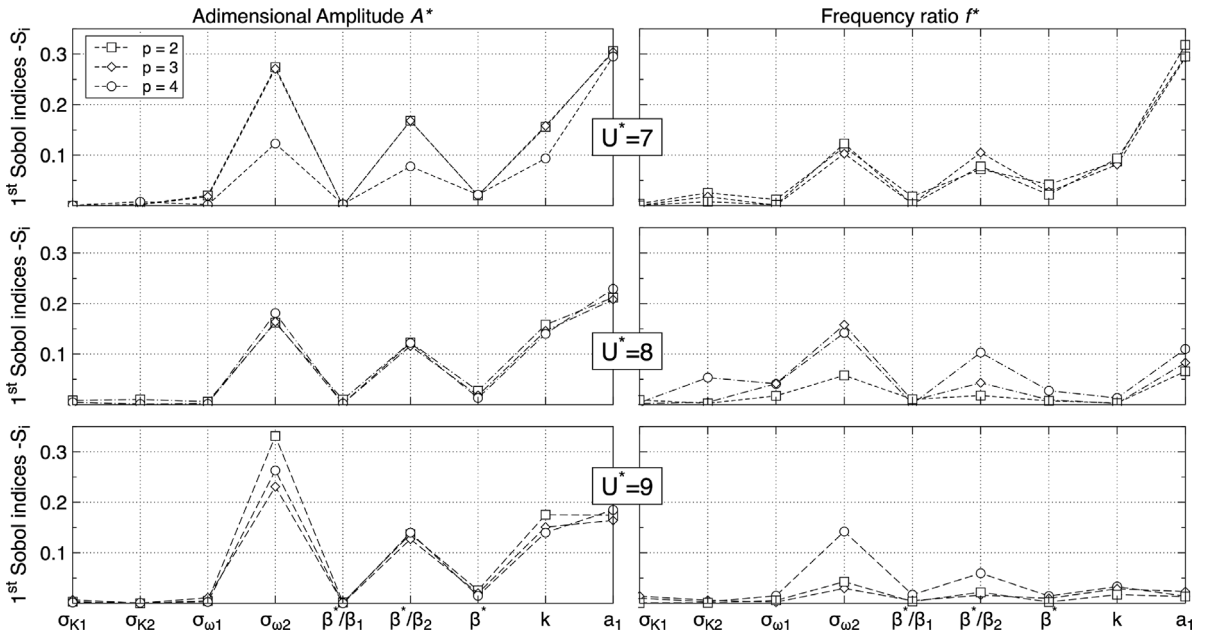

Fig. 5. First order Sobol indices S_i of the closure coefficients in the CCA.

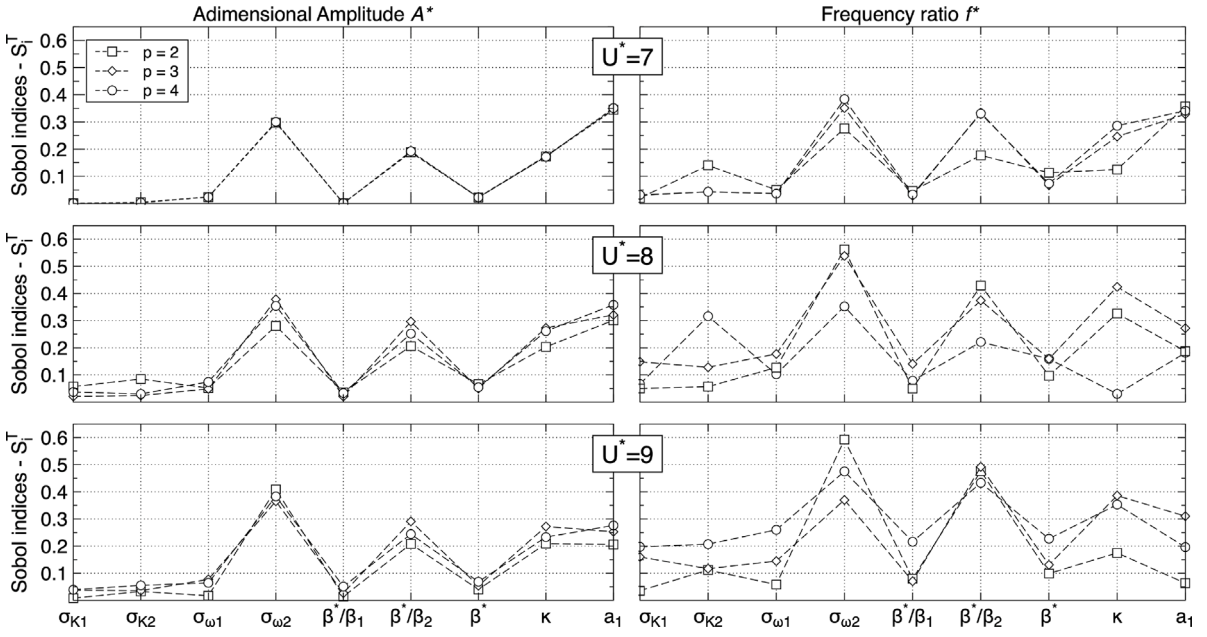

Fig. 6. Total sensitivity indices S_i^T of the closure coefficients in the CCA.

The main Sobol indices can clearly give a first indication of which are the most important input parameters, but can lead to misleading interpretations of the results (Homma and Saiteli, 1996).

For this reason, the total Sobol indices, S_i^T, are also considered. As exposed in Section 4.3, they provide a measure of the total effect of a given parameter, including all the possible interactions with the other parameters.

In this case, the interactions do not affect the rankings for A^*, as can be seen from Fig. 6. These rankings are consistent with those shown in Fig. 5 for main Sobol indices.

In case of f^*, the rankings are also in good agreement with those given for main Sobol indices in Fig. 6. However, for the sake of completeness, we point out that a discrepancy can be observed for $U^* = 8$ and $p = 2, 3$ where κ has a high score. In case of main Sobol indices this parameter shows a negligible contribution.

Table 7
$k-\omega$ SST closure coefficients and associated epistemic intervals used in the RDA.

Coefficient	Standard value	Lower bound	Upper bound
σ_{k_1}	0.85	0.7	1.0
σ_{ω_2}	0.856	0.7	1.0
β^*/β_2	1.0870	1.05	1.45
κ	0.41	0.38	0.42
a_1	0.31	0.31	0.40
σ_{k_2}	1.0	–	–
σ_{ω_1}	0.5	–	–
β^*/β_1	1.20	–	–
β^*	0.09	–	–

Table 8
Adimensional amplitude $A^* = A/D$ RDA results.

U^*	p	K.& W. (1996)	Base CFD	Mean	Std	Max	Min
7	4	≈ 0.577	0.520	0.556	0.034	0.666	0.480
	5			0.556	0.034	0.672	0.479
8	4	≈ 0.605	0.562	0.587	0.033	0.691	0.459
	5			0.587	0.031	0.697	0.451
9	4	≈ 0.610	0.606	0.626	0.035	0.738	0.508
	5			0.627	0.035	0.743	0.507

Table 9
Frequency ratio $f^* = f/f_0$ RDA results.

U^*	p	K.& W. (1996)	Base CFD	Mean	Std	Max	Min
7	4	≈ 1.258	1.294	1.331	0.017	1.389	1.312
	5			1.331	0.016	1.412	1.312
8	4	≈ 1.407	1.307	1.312	0.009	1.344	1.300
	5			1.312	0.008	1.350	1.300
9	4	≈ 1.392	1.346	1.297	0.009	1.331	1.288
	5			1.297	0.009	1.324	1.288

Analysing the two-way interactions, $S_{i,j}$, given in Fig. 7 for $p = 4$, it can be seen that, in the case of A^*, there is a clear contribution to the total indices from each of the pairs, $S_{i,j}$. In the case of the frequency, it can be seen that the contributions of $S_{\sigma_{\omega_2},\beta^*/\beta_2}$, $S_{\sigma_{\omega_2},\kappa}$ and $S_{\beta^*/\beta_2,\kappa}$ are not negligible for the flow regimes considered.

Finally, in Figs. 8 and 9 the overall interactions are compared. To clarify only the interactions with a value greater that 0.1 are labelled for convenience. From these graphs it is interesting to note that the fourth-order interactions increase with the increment of the reduced velocity.

All things considered, we have found that four closure coefficients provide a relevant contribution to uncertainty for the considered QoIs and flow regimes. These coefficients are: σ_{ω_2}, β^*/β_2, κ, a_1.

5.2. Reduced-dimensionality analysis (RDA)

Here, we also show the results of an RDA. The forward propagation of the uncertainty has been evaluated considering the most important parameters identified in previous CCA, plus a coefficient with a negligible impact (σ_{k1}).

The study has been, first, repeated for $p = 4$ and then extended to $p = 5$. Therefore, the total number of CFD evaluations was $N_s = 252$ for $p = 4$ and $N_s = 504$ for $p = 5$, respectively. Table 7 shows selected closure coefficients and ranges set according to Schaefer et al. (2015), along with the coefficients kept constant.

Considering the statistics reported in Tables 8 and 9 for U^* and f^*, respectively, it is possible to note that similar values have been obtained with $p = 4$ and $p = 5$. Moreover, as expected, the current results for $p = 4$ are in line with those of the CCA for the same polynomial order.

The ranking of the total indices, S_i^T, for both QoIs is given in Table 10, where the significant indices (those with value at least equal to $3 \cdot 10^{-2}$), are typed in black.

In this case, in order to visually appreciate the differences between the closure coefficients, the results of Table 10 are given in graphical form in Fig. 10. The good agreement between the results obtained with $p = 4$ and $p = 5$ confirms the ranking identified with the CCA.

The analyses of the interactions corresponding to A^* and f^* are shown in Figs. 11 and 12, respectively. In these figures, only the significant Sobol indices (i.e. value greater that 0.1) are highlighted in the plot for the sake of clarity. Several similarities can be observed among the model coefficient interactions for the three different flow regimes. For A^*, the largest contributions to the total sensitivity indices come from first-order Sobol indices, especially from S_{a1} and $S_{\sigma_{\omega_2}}$ for all the velocities.

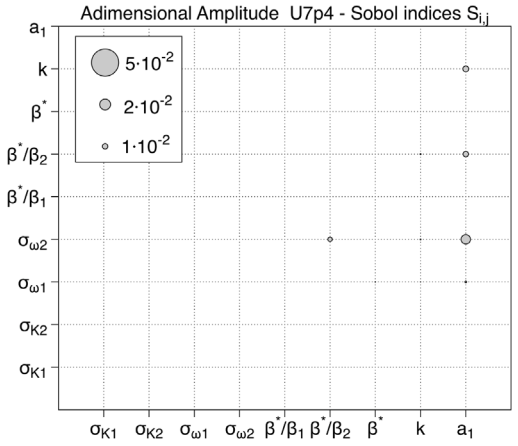

(a) $U^* = 7\ A^*$

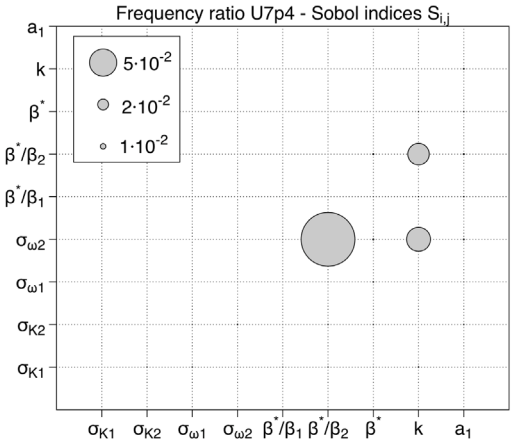

(b) $U^* = 7\ f^*$

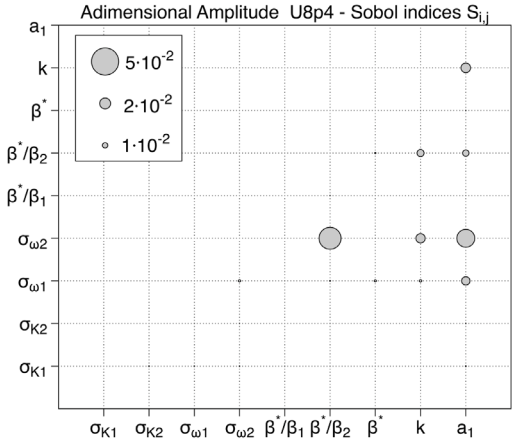

(c) $U^* = 8\ A^*$

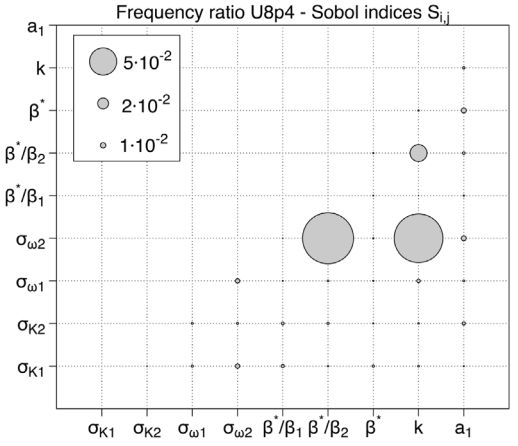

(d) $U^* = 8\ f^*$

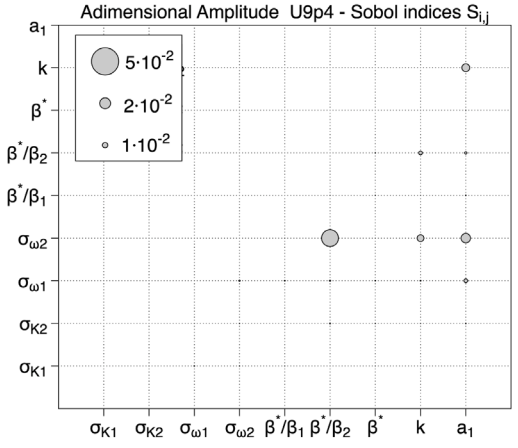

(e) $U^* = 9\ A^*$

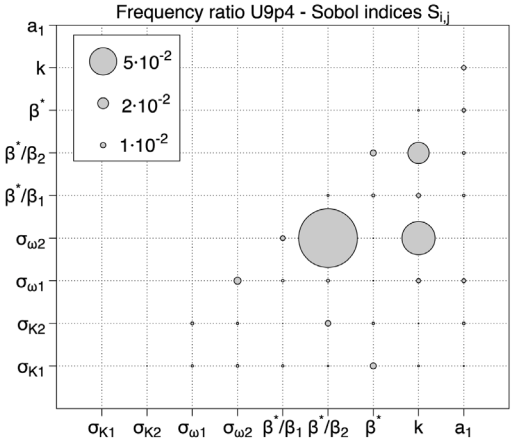

(f) $U^* = 9\ f^*$

Fig. 7. Second-order Sobol indices $S_{i,j}$ of the closure coefficients.

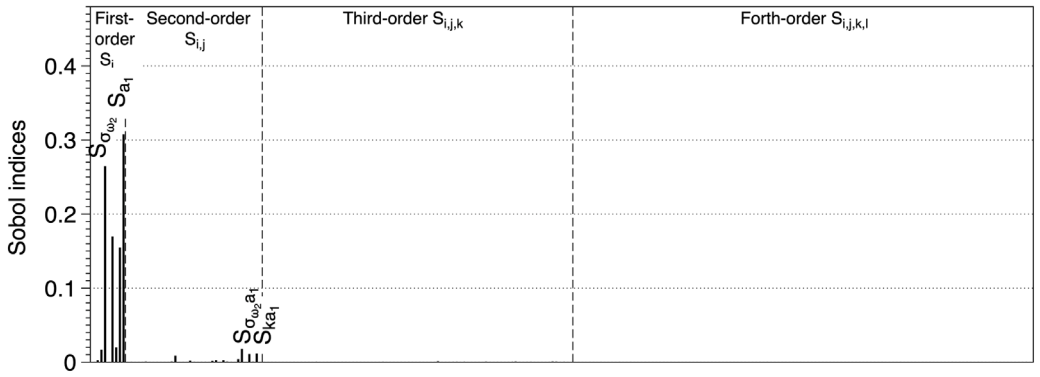

(a) $U^* = 7$

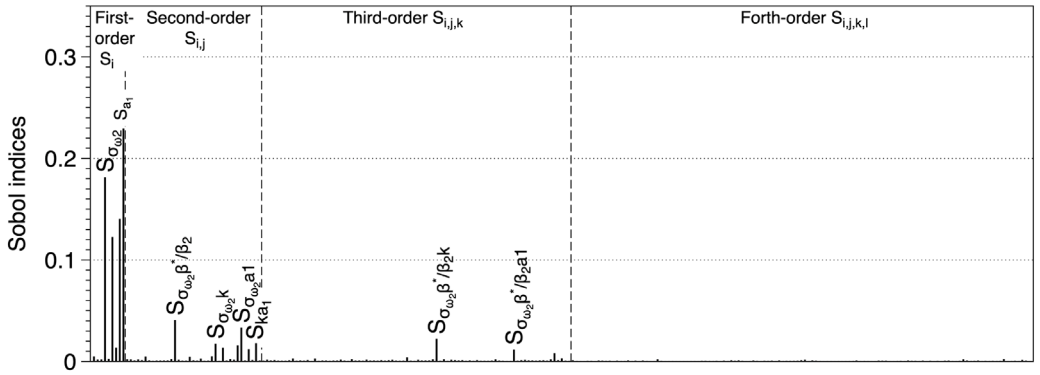

(b) $U^* = 8$

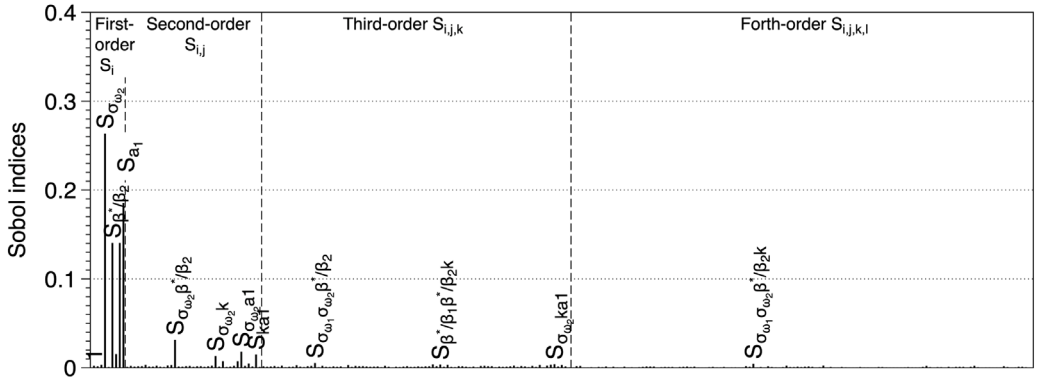

(c) $U^* = 9$

Fig. 8. Sobol sensitivity indices divided by single terms S_i, $S_{i,j}$, $S_{i,j,k}$ and $S_{i,j,k,l}$ for A^* ($p = 4$).

It is interesting to note that, in case of f^*, the two-way interactions sometimes exceed the first-order values.

These are: $S_{\sigma_{\omega_2}\beta^*/\beta_2}$, $S_{\sigma_{\omega_2}\kappa}$, $S_{\beta^*/\beta_2\kappa}$ and $S_{\sigma_{\omega_2}\beta^*/\beta_2\kappa}$. We therefore want to highlight the strong link between these three variables.

Finally, the overall results of the RDA confirms that the coefficients which can contribute to the uncertainty related to the predictions of A^* and f^* in the lower brach regime are: σ_{ω_2}, β^*/β_2, κ, a_1 and that as expected the coefficient σ_{k1} plays a negligible role.

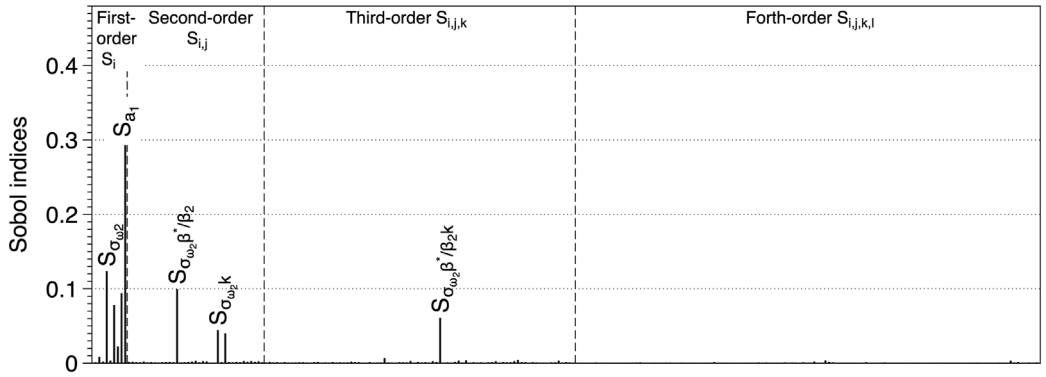

(a) $U^* = 7$

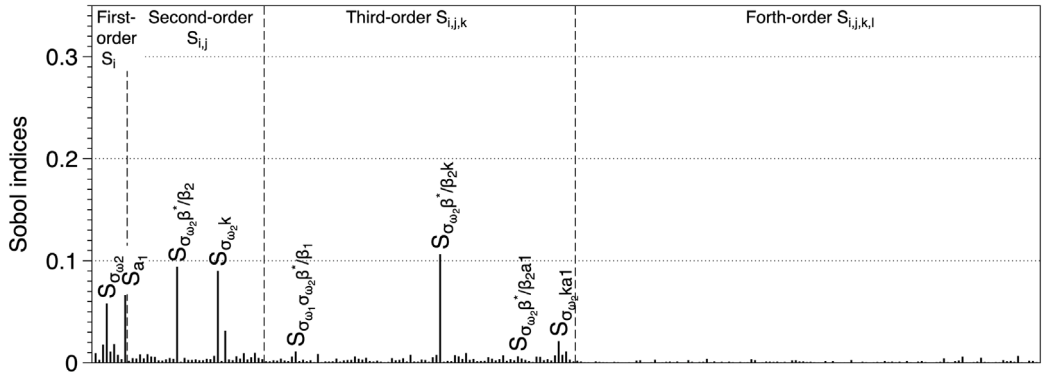

(b) $U^* = 8$

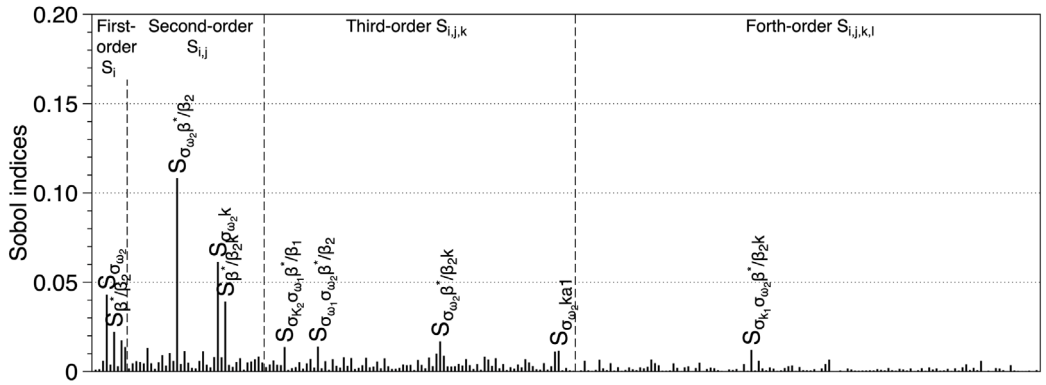

(c) $U^* = 9$

Fig. 9. Sobol sensitivity indices divided by single terms S_i, $S_{i,j}$, $S_{i,j,k}$ and $S_{i,j,k,l}$ for f^* $(p = 4)$.

6. Comparison with previous studies

In this section, we compare the list of the most significant coefficients identified in this study with those reported in some other selected studies. In particular in Table 11 we show the set obtained by Schaefer et al. (2015) for: an Axialsimmetric transonic Bump (ATB), a CFD case involving shock induced flow separation and a RAE2822 transonic problem. The second set refers to the study conducted by Erb and Hosder (2017) involving a 2D Zero pressure Gradient Flat Plate (2DZP). Finally, the list of Erb and Hosder

Table 10
Sobol total sensitivity indices of closure coefficients for the RDA. I-V denotes the ranking of significance. Gray text for Sobol indices less than $3 \cdot 10^{-1}$.

Index	Adimensional Amplitude A^*					
	$U^* = 7$		$U^* = 8$		$U^* = 9$	
	p=4	p=5	p=4	p=5	p=4	p=5
$S^T_{\sigma_{k_1}}$	0.0037(V)	0.0007(V)	0.0273(V)	0.0303(V)	0.0658(V)	0.0237(V)
$S^T_{\sigma_{\omega_2}}$	0.3221(II)	0.3159(II)	0.3922(I)	0.3924(I)	0.3927(I)	0.4522(I)
$S^T_{\beta^*/\beta_2}$	0.1996(III)	0.1944(II)	0.3002(III)	0.2839(III)	0.2343(IV)	0.2634(II)
S^T_{κ}	0.1777(IV)	0.1758(IV)	0.2571 (IV)	0.2506(IV)	0.2575(III)	0.2328(IV)
$S^T_{a_1}$	0.3594(I)	0.3678(I)	0.3232(II)	0.3440(II)	0.2813(II)	0.2582(III)
	Frequency ratio f^*					
	$U^* = 7$		$U^* = 8$		$U^* = 9$	
	p=4	p=5	p=4	p=5	p=4	p=5
$S^T_{\sigma_{k_1}}$	0.0770(V)	0.0636(V)	0.0825(V)	0.1165(V)	0.0953(V)	0.0982(V)
$S^T_{\sigma_{\omega_2}}$	0.4409(I)	0.4099(I)	0.7406(I)	0.7219(I)	0.7505(I)	0.7317(I)
$S^T_{\beta^*/\beta_2}$	0.4047(II)	0.4097(II)	0.5850(II)	0.5592(II)	0.5226(II)	0.5717(II)
S^T_{κ}	0.3158(IV)	0.3426(IV)	0.4274(III)	0.2839(III)	0.3871(III)	0.4983(III)
$S^T_{a_1}$	0.3493(III)	0.4027(III)	0.1451(IV)	0.2072(IV)	0.1245(IV)	0.1355(IV)
$(P_m + 1)$	126	252	126	252	126	252
N_s	252	504	252	504	252	504

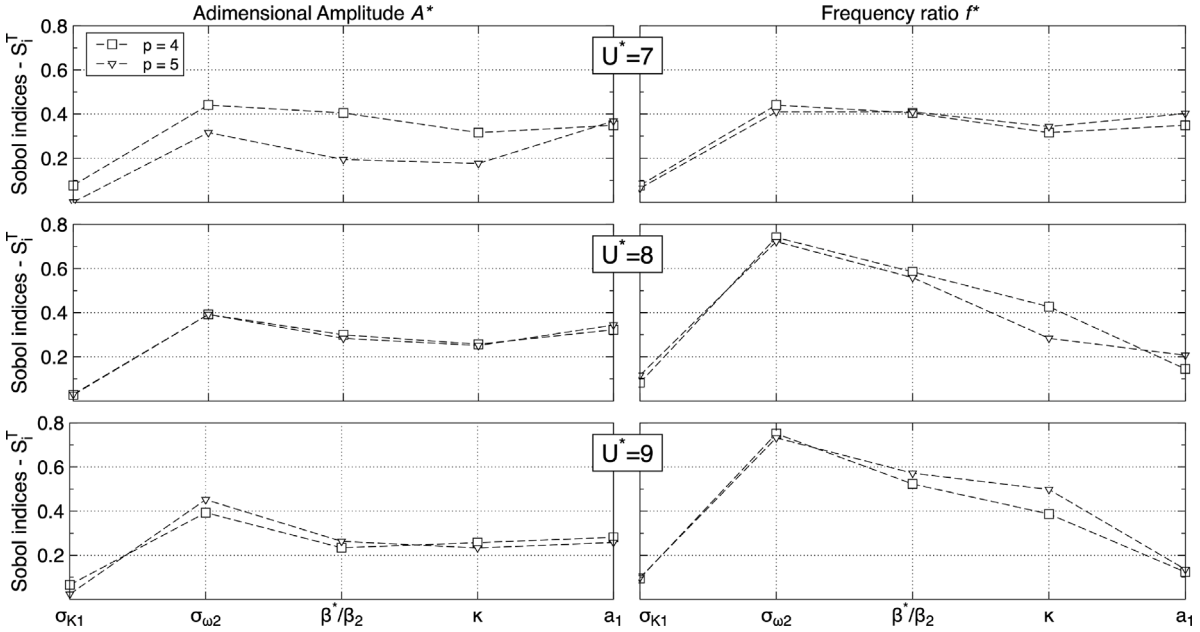

Fig. 10. Total sensitivity indices S_i^T of the closure coefficients in the RDA.

(2018) is for a study conducted involving an Axisymmetric Shock Wave Boundary Layer interaction (ASWBLI), the validation case including an axisymmetric cylindrical body with a training edge flare of 20 degrees at an upstream Mach number of 7.11.

From Table 11, it can be observed that there is no a common set between the different studies. Each of the coefficients, β^*/β_2 and a_1 play an important role in four of the five cases studied. The coefficients β^*, σ_{ω_1} and σ_{ω_1} plays a significant role for three of the cases studied. Finally, the coefficient κ is significant only for two cases studied. Therefore, it seems that the $k-\omega$ SST turbulence model is very sensitive, through its closing coefficients, to the type of numerical simulation to be solved, which justify the effort of the current study.

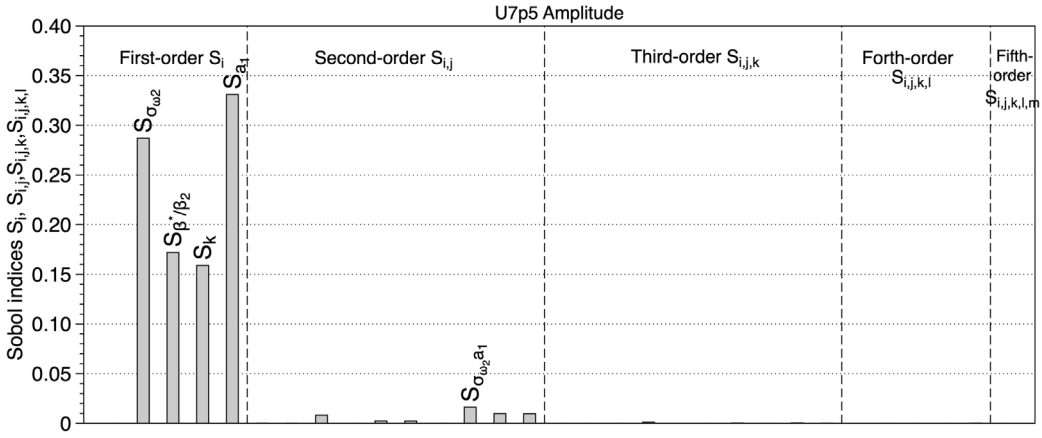

(a) $U^* = 7$

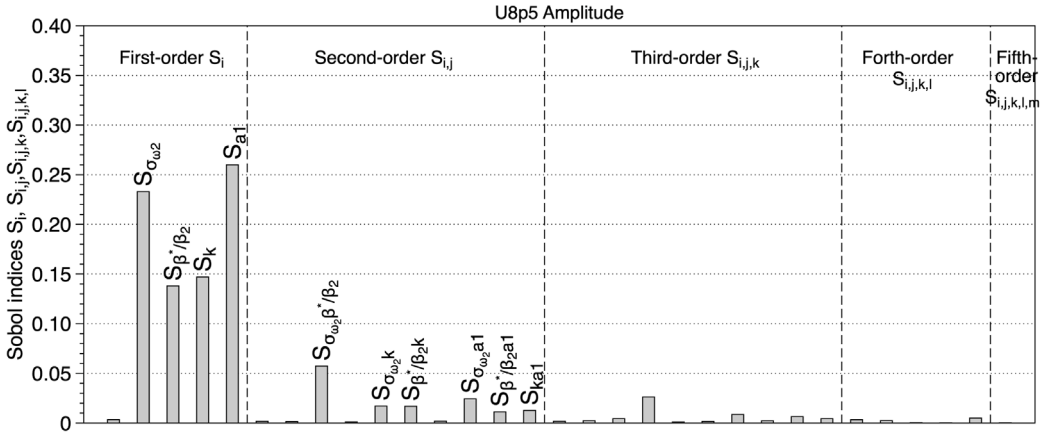

(b) $U^* = 8$

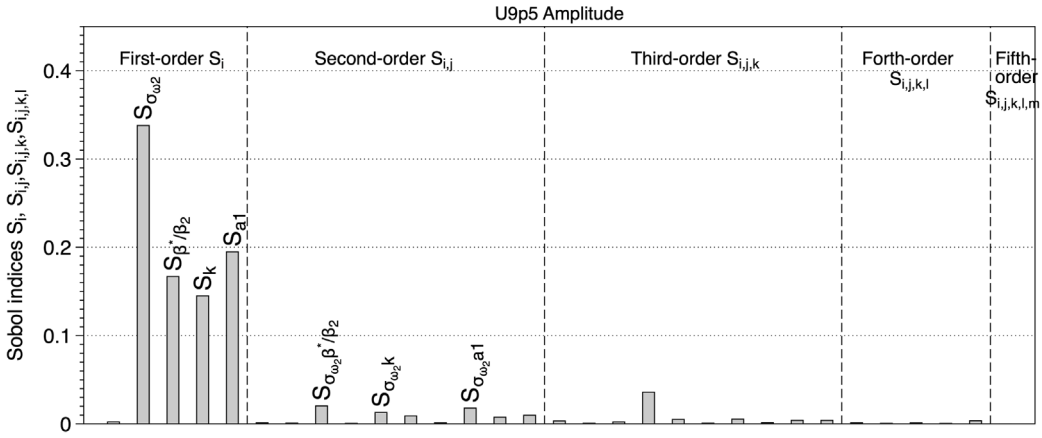

(c) $U^* = 9$

Fig. 11. Sobol sensitivity indices divided by single terms S_i, $S_{i,j}$, $S_{i,j,k}$, $S_{i,j,k,l}$ and $S_{i,j,k,l,m}$ for A^* in the RDA ($p = 5$).

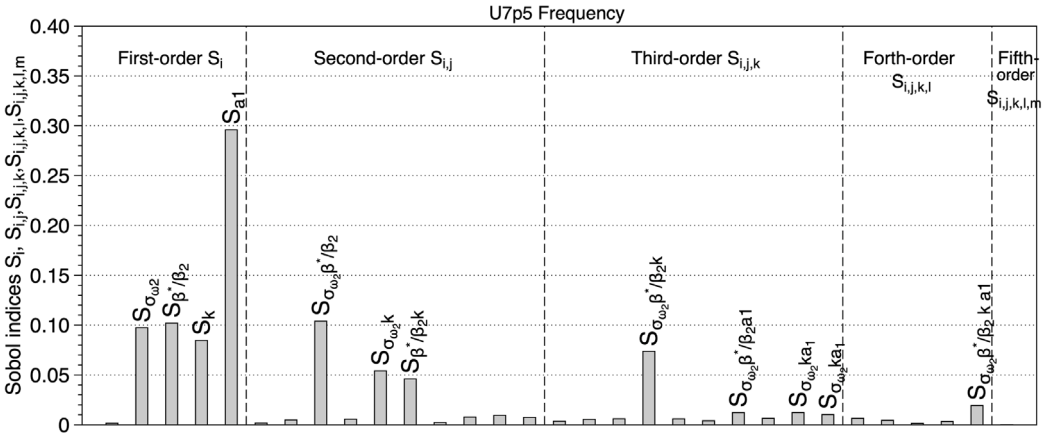

(a) $U^* = 7$

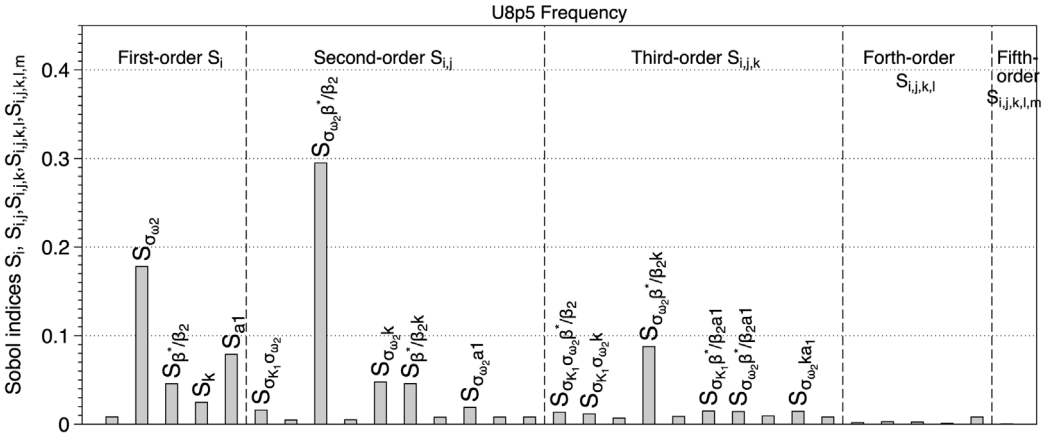

(b) $U^* = 8$

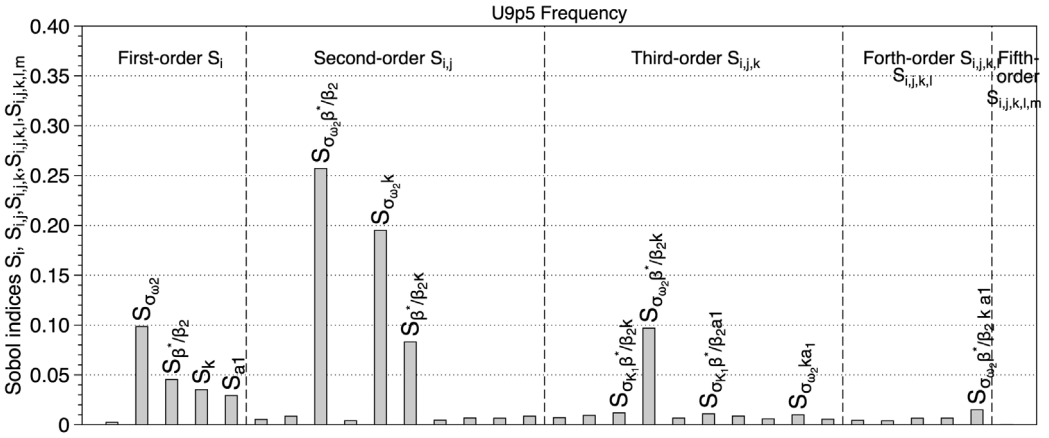

(c) $U^* = 9$

Fig. 12. Sobol sensitivity indices divided by single terms S_i, $S_{i,j}$, $S_{i,j,k}$, $S_{i,j,k,l}$ and $S_{i,j,k,l,m}$ for f^* in the RDA ($p = 5$).

Table 11
Comparison between present and previous studies of significant closure coefficients in the $k-\omega$ SST model.

Authors	Case	Coefficients
Schaefer et al. (2015)	ATB	β^*, σ_{ω_1}, β^*/β_1, β^*/β_2, a_1
	RAE2822	β^*, σ_{ω_1}, β^*/β_2, a_1
Erb and Hosder (2017)	2DZP	β^*, σ_{ω_2}, β^*/β_1
Erb and Hosder (2018)	ASWBLI	σ_{ω_1}, σ_{ω_2}, β^*/β_2, κ, a_1
Present	2D VIV	σ_{ω_2}, β^*/β_2, κ, a_1

7. Conclusions

In this study the uncertainty quantification study and sensitivity analysis for the $k-\omega$ SST turbulence model due to the epistemic uncertainty in closure coefficients for bi-dimensional simulation of VIV for a circular cylinder with 1-DOF has been presented.

The study has been carried out using the non-intrusive polynomial chaos approach in combination with the Sobol indices used to rank the contribution of closure coefficients to the total uncertainty in the output quantities of interest (adimensional amplitude and frequency ratio). The required simulations have been performed using a native URANS solvers available in OpenFOAM library. The overall computational framework has been driven by DAKOTA.

The results of the current study identify a set of four coefficients that contribute most to uncertainty quantities. These are σ_{ω_2}, β^*/β_2, κ and a_1. The findings of the present study have been compared with the results provided by some other selected works (Schaefer et al., 2015; Erb and Hosder, 2017, 2018). From this comparison has not been identified a common list of most significant coefficients.

For this reason, the present study aims to contribute to the improving of the knowledge of the parametric uncertainty of these closure coefficients in URANS simulations for flow problems including the vortex-induced vibrations on circular cylinders.

CRediT authorship contribution statement

Simone Martini: Writing – review & editing, Writing – original draft, Visualization, Validation, Software, Methodology, Investigation, Formal analysis, Data curation, Conceptualization. **Mitja Morgut:** Writing – review & editing, Writing – original draft, Supervision, Software, Methodology, Investigation, Formal analysis, Conceptualization. **Riccardo Pigazzini:** Writing – review & editing, Writing – original draft, Methodology, Formal analysis. **Lucia Parussini:** Writing – review & editing, Investigation.

Declaration of competing interest

The authors declare that they have no known competing financial interests or personal relationships that could have appeared to influence the work reported in this paper.

Acknowledgements

This work was partly performed in the context of the UBE 2 (Underwater Blue Efficiency 2) project supported by the Regional Program POR FESR 2014 2020, 1.3.b – Bando DGR 1489/2017, Ricerca e sviluppo – Aree di specializzazione tecnologie marittime e smart health of Regione Friuli-Venezia Giulia, Italy.

Appendix. The Menter shear stress transport model as implemented in OpenFOAM

The OpenFOAM (v.2.4) implemented version of the $k-\omega$ SST model is a variant of the original model presented by Menter in 1994 (Menter, 1994). The OpenFOAM variant considers the improvements proposed by Menter and Esch (Menter and Esch, 2001) with the updated coefficients from Menter et al. (2003b) but with the consistent production terms from the Menter and Esch (2001) paper[2] and the addition of a new term that considers the rough walls, as proposed by Hellsten (1997).

The idea behind the Menter SST model is to combine the different elements of the existing eddy viscosity model that are superior to their alternatives. In particular, the model retains the robust and accurate formulation of the Willcox $k-\omega$ model in the near wall region and takes the advantage of the $k-\varepsilon$ model in the outer part of the boundary layer. To achieve this, first of all the $k-\varepsilon$ model is transformed into a $k-\omega$ formulation defining the ω in terms of k and ε:

$$\omega = \frac{\varepsilon}{\beta^* k}, \qquad \beta^* = C_\mu, \tag{A.1}$$

where $C_\mu = 0.09$ is the constant present in the expression for the turbulent viscosity in the $k-\varepsilon$ model.

[2] As noted by the Largley Research Center (NASA Langley Research Center, 2021) in the Menter et al. (2003b) articles there is a typo in the omega equation therefore in OpenFOAM is implemented the corrected version.

Then the transformed $k-\varepsilon$ model is merged with the original $k-\omega$ formulation with the help of a function F_1. In detail, the original $k-\omega$ model is multiplied by F_1 and the transformed $k-\varepsilon$ model by $(1-F_1)$, and both added together. The function F_1 is designed to be one in the near wall region (activating the original $k-\omega$ model) and zero away from the surface. The resulting equation for k and ω are as follows:

$$\frac{D\rho k}{Dt} = P - \beta^*\rho k\omega + \frac{\partial}{\partial x_j}\left[(\mu + \sigma_k\mu_T)\frac{\partial k}{\partial x_j}\right], \tag{A.2}$$

$$\frac{D\rho\omega}{Dt} = \frac{\gamma\rho}{\mu_T}P - \beta\rho\omega^2 + \frac{\partial}{\partial x_j}\left[(\mu + \sigma_\omega\mu_T)\frac{\partial\omega}{\partial x_j}\right] + 2\rho\frac{(1-F_1)\sigma_{\omega_2}}{\omega}\frac{\partial k}{\partial x_j}\frac{\partial\omega}{\partial x_j}. \tag{A.3}$$

The left hand side of the previous equations is the Lagrangian derivative: $D/Dt = \partial/\partial t + u_i\partial/\partial x_i$. Note that the OpenFOAM implementation is written in terms of σ diffusion coefficient rather than the more traditional fraction of σ (Hellsten, 1997) ($\sigma = 1/\sigma_{orig}$) so that the bending can be applied to all coefficients in a consistent manner. The model constants in Eqs. (A.2) and (A.3) are evaluated from

$$\sigma_k = F_1\sigma_{k_1} + (1-F_1)\sigma k_2, \tag{A.4}$$

$$\sigma_\omega = F_1\sigma_{\omega_1} + (1-F_1)\sigma\omega_2, \tag{A.5}$$

$$\beta = F_1\beta_1 + (1-F_1)\beta_2, \tag{A.6}$$

$$\gamma = F_1\gamma_1 + (1-F_1)\gamma_2, \tag{A.7}$$

where subscripts 1 and 2 refer to constants in Wilcox's model and the transformed $k-\varepsilon$ model, respectively. The constraints of the original $k-\omega$ model (corresponding to set 1) have the following values:

$$\begin{aligned} &\sigma_{k_1} = 0.85, \qquad \sigma_{\omega_1} = 0.5, \qquad \beta_1 = 0.075, \\ &\beta^* = 0.09, \qquad \kappa = 0.41, \qquad \gamma_1 = \beta_1/\beta^* - \sigma_{\omega_1}\kappa^2/\sqrt{\beta^*} \approx 5/9. \end{aligned} \tag{A.8}$$

The constraints of the transformed $k-\varepsilon$ model (corresponding to set 2) have the following value:

$$\begin{aligned} &\sigma_{k_2} = 1.0, \qquad \sigma_{\omega_2} = 0.856, \qquad \beta_1 = 0.0828, \\ &\beta^* = 0.09, \qquad \kappa = 0.41, \qquad \gamma_2 = \beta_2/\beta^* - \sigma_{\omega_2}\kappa^2/\sqrt{\beta^*} \approx 0.44. \end{aligned} \tag{A.9}$$

In Eqs. (A.2) and (A.3), P is the production of the kinetic energy of turbulence and is modelled using the Boussinesq approximation as follows:

$$P = (2\mu_T E_{ij} - \frac{2}{3}\delta_{ij}\rho k)\frac{\partial u_i}{\partial x_j}, \tag{A.10}$$

where $E_{ij} = (\partial u_i/\partial x_j + \partial u_j/\partial x_i)/2$ is the strain rate tensor. Menter suggested (Menter et al., 2003a) replacing the term P with $\tilde{P}$, where $\tilde{P}$ is the limiter to prevent the build-up of turbulence stagnation region:

$$\tilde{P} = min\left(P, c_1\beta^*\rho k\omega\right). \tag{A.11}$$

Therefore, Eq. (A.11) does not change the solution but only eliminates the occurrence of spikes in the eddy-viscosity due to numerical "wiggles" in the shear-strain tensor. The constant c_1 in the Eq. (A.11) is fixed to 10 after the upgraded version of Hellsten (1997)

The last term in the ω-equation (Eq. (A.3)) originates from the transformed ε-equation and is called "the cross diffusion term". This term makes the model from insensitive to free-stream ω.

The blending function F_1 is given by

$$F_1 = \tanh(\Gamma_1^4), \tag{A.12}$$

where

$$\Gamma_1 = min\left(max\left(\frac{\sqrt{k}}{\beta^*\omega d}; \frac{500\nu}{\omega d^2}\right); \frac{4\rho\sigma_{\omega_2}k}{CD_{k\omega}d^2}\right). \tag{A.13}$$

The term Γ_1 goes to zero far away from solid surfaces because of the wall-distance d dependency ($1/d$ or $1/d^2$) in all three terms in Eq. (A.13). Inside a boundary layer the three arguments in Eq. (A.13) have the following purpose: the first term is the turbulent length scale divided by the wall-distance d. This ratio is about 2.5 in the log-layer and tends towards zero in the deflect layer. The second term exceeds unity only in the sublayer. The third term is an additional safeguard argument designed to ensure correct behaviour of F_1 in cases of very low free-stream ω. $CD_{k\omega}$ is the positive portion of the cross-diffusion term

$$CD_{k\omega} = max\left(\frac{2\rho\sigma_{\omega_2}}{\omega}\frac{\partial k}{\partial x_j}\frac{\partial\omega}{\partial x_j}; 10^{-10}\right). \tag{A.14}$$

The eddy viscosity formula μ_T, with the modification of Hollisten (Hellsten, 1997), is defined by

$$\mu_T = \frac{a_1\rho k}{max(a_1\omega; b_1|E_{ij}|F_2F_3)}, \tag{A.15}$$

Table A.12
$k-\omega$ SST coefficients descriptions.

Coefficient	Description
$CD_{k\omega}$	Positive portion of the cross-diffusion term in ω-transport equation
P	Production of the kinetic energy of turbulence
a_1	Bradshaw's structural parameter used in the eddy viscosity definition
b_1	Constant factor in the turbulent viscosity equation
c_1	Constant factor in the production limiter
$F_1,\ F_2,\ F_3$	Auxiliary functions in turbulence model
δ_{ij}	Kroneker's delta
μ	Dynamic viscosity
μ_T	Turbulent viscosity
$\sigma_{k_1}, \sigma_{k_2}$	Turbulence-model coefficient in k-equation[a]
$\sigma_{\omega_1}, \sigma_{\omega_2}$	Turbulence-model coefficient in ω-equation
$\beta_1,\ \beta_2$	Turbulence-model coefficients used in the calculation of β for ω-equation
$\beta^*/\beta_1,\ \beta^*/\beta_2$	Blended ratio approximates the time decay of homogeneous isotropic turbulence experiments.
β^*	Turbulence-model coefficient that multiplies $k\omega$ in k-equation of the model
$\gamma_1,\ \gamma_2$	Coefficients involved in log calibration
$\Gamma_1,\ \Gamma_2$	Auxiliary variable in turbulence model

[a] Values chosen to match empirical decay rate of k and μ_T as wall distance increases.

where $|E_{ij}| = \sqrt{2E_{ij}E_{ij}}$ is the scalar measure of the strain-rate tensor E_{ij}. The function F_2 in Eq. (A.15) is to prevent the activation of the SST limitation in free shear flows. F_2 becomes one for boundary layer flows and zero for free shear layers. The formula of F_2 is given by

$$F_2 = \tanh(\Gamma_2^2), \tag{A.16}$$

where

$$\Gamma_2 = max\left(\frac{2\sqrt{k}}{\beta^*\omega d}; \frac{500\nu}{\omega d^2}\right). \tag{A.17}$$

The function F_3 is designed to prevent the SST limitation from being activated in the roughness layer in rough-wall flows. This function is necessary because Brashaw's assumption is not valid there. The function F_3 is given by

$$F_3 = 1 - \tanh\left[\left(\frac{150\nu}{\omega d^2}\right)^4\right] \tag{A.18}$$

In order to finally summarize all coefficients used in the Menter SST turbulence model Table A.12 is presented. In Table A.12 for each coefficient used, a brief explanation of their functions is also provided.

Data availability

Data will be made available on request.

References

Al-Jamal, H., Dalton, C., 2004. Vortex induced vibrations using large eddy simulation at a moderate Reynolds number. J. Fluids Struct. 19 (1), 73–92.
Bernitsas, M.M., Raghavan, K., Ben-Simon, Y., Garcia, E., 2008. VIVACE (vortex induced vibration aquatic clean energy): A new concept in generation of clean and renewable energy from fluid flow. J. Offshore Mech. Arct. Eng. 130 (4), 041101.
Bigoni, D., 2015. Uncertainty Quantification with Applications to Engineering Problems (Ph.D. thesis). Technical University of Denmark.
Blackburn, H.M., Govardhan, R., Williamson, C., 2001. A complementary numerical and physical investigation of vortex-induced vibration. J. Fluids Struct. 15 (3–4), 481–488.
Drumond, G.P., Pasqualino, I.P., Pinheiro, B.C., Estefen, S.F., 2018. Pipelines, risers and umbilicals failures: A literature review. Ocean Eng. 148, 412–425.
Eldred, M., Giunta, A., Brown, S., Adams, B., Dunlavy, D., Eddy, J., Gay, D., Griffin, J., Hart, W., Hough, P., Kolda, T., Martinez-Canales, M., Swiler, L., Watson, J., Williams, P., 2006. DAKOTA, A Multilevel Parallel Object-Oriented Framework for Design Optimization, Parameter Estimation, Uncertainty Quantication, and Sensitivity Analysis. Version 4.0 Reference Manual.
Erb, A., Hosder, S., 2017. Uncertainty analysis of turbulence model closure coecients for wall-bounded attached and separated flows. In: 19th AIAA Non-Deterministic Approaches Conference AIAA Paper 2017–2018.
Erb, A., Hosder, S., 2018. Uncertainty analysis of turbulence model closure coecients for shock wave-boundary layer interaction simulations. In: AIAA Aerospace Sciences Meeting.
Ghanem, R., Higdon, D., Owhadi, H., 2017. Handbook of Uncertainty Quantification. Springer.

Guilmineau, E., Queutey, P., 2004. Numerical simulation of vortex-induced vibration of a circular cylinder with low mass-damping in a turbulent flow. J. Fluids Struct. 19 (4), 449–466.
Hellsten, A., 1997. Some Improvements in Menter's k - w SST Turbulence Model. In: 29th AIAA Fluid Dynamics Conference, vol. AIAA-98-2554.
Hobbs, W.B., Hu, D.L., 2012. Tree-inspired piezoelectric energy harvesting. J. Fluids Struct. 28, 103–114.
Homma, T., Saiteli, A., 1996. Importance measures in global sensitivity analysis of nonlinear models. Reliab. Eng. Syst. Saf. 52, 1–17.
Hosder, S., Walters, R., Balch, M., 2010. Point-collocation nonintrusive polynomial chaos method for stochastic computational fluid dynamics. AIAA J. 48 (12).
Khalak, A., Williamson, C., 1996. Dynamics of a hydroelastic cylinder with very low mass and damping. J. Fluids Struct. 10 (5), 455–472.
Le Cunff, C., Biolley, F., Fontaine, E., Etienne, S., Facchinetti, M., 2002. Vortex-induced vibrations of risers: Theoretical, numerical and experimental investigation. Oil Gas Sci. Technol. 57, 59–69. http://dx.doi.org/10.2516/ogst:2002004.
Li, T., Ishihara, T., 2021. Numerical study on vortex-induced vibration of circular cylinder with two-degree-of-freedom and geometrical nonlinear system. J. Fluids Struct. 107, 103415.
Löhner, R., Yang, C., 1996. Improved ALE mesh velocities for moving bodies. Commun. Numer. Methods Eng. 599–608.
Lucor, D., Foo, J., Karniadakis, G., 2005. Vortex mode selection of a rigid cylinder subject to VIV at low mass-damping. J. Fluids Struct. 20 (4), 483–503.
Lysenko, D., Ertesvag, I., Rian, K., 2014. Large-eddy simulation of the flow over a CircularCylinder at Reynolds number 2×10^4. Flow Turbul. Combust. 92 (3), 673–698.
Martini, S., 2020. Numerical Investigation of One-Degree-Of-Freedom Vortex-Induced Vibration of a Rigid Circular Cylinder (Ph.D. thesis). University of Trieste, URL: https://arts.units.it/handle/11368/2973221.
Martini, S., Morgut, M., Pigazzini, R., 2021. Numerical VIV analysis of a single elastically-mounted cylinder: Comparison between 2D and 3D URANS simulations. J. Fluids Struct. 104, 103303.
Menter, F., 1994. Two-equation eddy-viscosity turbulence models for engineering applications. AIAA J. 32 (8).
Menter, F., Esch, T., 2001. Elements of industrial heat transfer predictions. In: 16th Brasilian Congress of Mechanical Engineering.
Menter, F.R., Kuntz, M., Bender, R., 2003a. A scale-adaptive simulation model for turbulent flow prediction. In: AIAA 2003-0767 41st Aerospace Science Meeting and Exhibit. Reno, Nevada.
Menter, F., Kuntz, M., Langtry, R., 2003b. Ten years of industrial experience with the SST turbulence model. In: Proceedings of the Fourth International Symposium on Turbulence, Heat and Mass Transfer, vol. 4, pp. 625–632.
NASA Langley Research Center, 2021. The Wilcox k-omega turbulence model. URL: https://turbmodels.larc.nasa.gov/wilcox.html.
Pan, Z., Cui, W., Miao, Q., 2007. Numerical simulation of vortex-induced vibration of a circular cylinder at low mass-damping using RANS code. J. Fluids Struct. 23 (1), 23–37.
Pastrana, D., Cajas, J., Lehmkuhl, O., Rodríguez, I., Houzeaux, G., 2018. Large-eddy simulations of the vortex-induced vibration of a low mass ratio two-degree-of-freedom circular cylinder at subcritical Reynolds numbers. Comput. & Fluids 173, 118–132.
Pigazzini, R., 2016. Analysis of 2D VIV of Two Circular Cylinders in Tandem Arrangement by an Open-Source CFD Solver (Master's thesis). Dept. of Engineering and Architecture, University of Trieste.
Pigazzini, R., Contento, G., Martini, S., Puzzer, T., Morgut, M., Mola, A., 2018. VIV analysis of a single elastically-mounted 2D cylinder: Parameter identification of a single-degree-of-freedom multi-frequency model. J. Fluids Struct. 78, 299–313.
Rezaeiravesh, S., Vinuesa, R., Schlatter, P., 2022. An uncertainty-quantification framework for assessing accuracy, sensitivity, and robustness in computational fluid dynamics. J. Comput. Sci. 62.
Saltara, F., Neto, A.D., Lopez, J.I.H., 2011. 3D CFD simulation of vortex-induced vibration of cylinder. Int. J. Offshore Polar Eng. 21 (2), 1–6.
Schaefer, J., Westy, T., Hosderz, S., Rumsey, C., Carlson, J.-R., Klebk, W., 2015. Uncertainty quanti cation of turbulence model closure coecients for transonic wall-bounded flows. In: 22nd AIAA Computational Fluid Dynamics Conference.
Soize, C., 2017. Uncertainty Quantification. Springer.
Soti, A.K., Thompson, M.C., Sheridan, J., Bhardwaj, R., 2017. Harnessing electrical power from vortex-induced vibration of a circular cylinder. J. Fluids Struct. 70, 360–373.
Sudret, B., 2008. Global sensitivity analysis using polynomial chaos expansions. Reliab. Eng. Syst. Saf. 93, 964–979.
Sudret-2008, 2008. Global sensitivity analysis using polynomial chaos expansions. Reliab. Eng. Syst. Saf. 93 (7), 964–979.
Sullivan, T., 2015. Introduction to Uncertainty Quantification. Springer.
Wanderley, J., Souza, G., Sphaier, S., Levi, C., 2008. Vortex-induced vibration of an elastically mounted circular cylinder using an upwind TVD two-dimensional numerical scheme. Ocean Eng. 35 (14), 1533–1544.
Weaver, D.t., Fitzpatrick, J., 1988. A review of cross-flow induced vibrations in heat exchanger tube arrays. J. Fluids Struct. 2 (1), 73–93.
West, T.K., Hosder, S., 2015. Uncertainty quanti cation of hypersonic reentry flows with sparse sampling and stochastic expansions. J. Spacecr. Rockets 52 (1), 120–133.
Wojtkiewicz, S., Eldred, M.S., Field, R., Urbina, J.A., Red-Horse, J., 2001. Uncertainty quantification in large computational engineering models. In: Proceedings of the 42nd AIAA/ASME/ASCE/AHS/ASCStructures, Structural Dynamics, and Materials Conference, AIAA Paper No. 2001-1455.
Wu, W., Bernitsas, M.M., Maki, K., 2014. RANS simulation versus experiments of flow induced motion of circular cylinder with passive turbulence control at 35,000 < RE < 130,000. J. Offshore Mech. Arct. Eng. 136 (4), 041802.
Xia, L., Zou, Z.-L., Wang, Z.-H., Zou, L., Gao, H., 2021. Surrogate model based uncertainty quantification of CFD simulations of the viscous flow around a ship advancing in shallow water. Ocean Eng. 234.
Xiao, H., Cinella, P., 2019. Quantification of model uncertainty in RANS simulations: A review. Prog. Aerosp. Sci. 108, 1–31.
Xiu, D., 2010. Numerical Methods for Stochastic Computations: A Spectral Method Approach. Princeton University Press.
Yin, D., Passano, E., Jiang, F., Lie, H., Wu, J., Ye, N., Sævik, S., Leira, B.J., 2022. State-of-the-art review of vortex-induced motions of floating offshore wind turbine structures. J. Mar. Sci. Eng. 10 (8), 1021. http://dx.doi.org/10.3390/jmse10081021.
Zheng, H., Price, R.E., Modarres-Sadeghi, Y., Triantafyllou, M.S., 2014. On fatigue damage of long flexible cylinders due to the higher harmonic force components and chaotic vortex-induced vibrations. Ocean Eng. 88, 318–329.